

Microstructure evolution and mechanical characterization of friction stir welded titanium alloy Ti–6Al–4V using lanthanated tungsten tool

P. M. Mashinini^a, I. Dinaharan^{b*}, J. David Raja Selvam^a, D.G. Hattingh^c

^aDepartment of Mechanical and Industrial Engineering, University of Johannesburg, Doornfontein Campus, Johannesburg 2028, South Africa.

^bDepartment of Mechanical Engineering Science, University of Johannesburg, Auckland Park Kingsway Campus, Johannesburg 2006, South Africa.

^cDepartment of Mechanical Engineering, Nelson Mandela Metropolitan University, Port Elizabeth 6001, South Africa.

*Corresponding author.

E-mail addresses: mmashinini@uj.ac.za (P. M. Mashinini), dinaweld2009@gmail.com (I.

Dinaharan), jdavidselvam@gmail.com (J. David Raja Selvam), danie.hattingh@[nmmu.ac.za](mailto:hattingh@nmmu.ac.za)

(D.G. Hattingh).



Abstract

Friction stir welding (FSW) exhibits significant advantages to join titanium and its alloys compared to other welding methods. FSW of 3 mm thick titanium alloy Ti–6Al–4V sheets was carried out using a lanthanated tungsten alloy tool. The traverse speed was varied from 40 mm/min to 200 mm/min in steps of 80 mm/min by keeping other parameters constant. The microstructure evolution was observed using conventional and advanced characterization techniques. The micrographs revealed a fully developed lamellar structure at 40 mm/min and a recrystallized structure in rest of the joints. An increase in β phase was observed at HAZ while TMAZ showed a distorted structure. The average grain size was observed to reduce with an increase in traverse speed. No tool wear debris was observed in the stir zone while a worm hole defect was noticed at 200 mm/min. Ti–6Al–4V hardened

after FSW due to grain refinement and dislocation density. The joint strength was closer to the strength of base metal and the joints failed outside joint area except at 200 mm/min.

Key words: Titanium alloy; Friction stir welding; Microstructure; Tensile Strength.

1. Introduction

Titanium and its alloys are well recognized and applied in numerous industries because of desirable properties including as high specific strength, outstanding corrosion resistance, improved biocompatibility, elevated temperature resistance, superior fatigue and cracking resistance [1–4]. One of the titanium alloys Ti–6Al–4V is considered as the workhorse of aerospace and aeronautical industries due to major use in key components. Welding of titanium alloys is a primary requirement for applications in structures and components. They can be readily joined by means of traditional and high energy welding processes including gas tungsten arc welding [5], plasma arc welding [6], electron beam welding [7] and laser beam welding [8]. The joints were often characterized by non–aesthetic bead, porosity, coarse microstructure, reduced ductility, residual stress, cracking and distortion [9–12]. Solid state welding processes are capable of overcoming those undesirable characteristics. High performance titanium joints were demonstrated using linear friction welding [13] and conventional friction welding [14]. Nevertheless, those processes are applicable only to specific geometric shapes and an additional arrangement to remove the flashes is required.

Friction stir welding (FSW) has emerged as a viable solid state joining method for titanium and its alloys to overcome the setbacks of other welding processes. FSW was originally conceived at TWI in 1991 to weld light weight aluminum alloys [15,16]. Frictional heat and plastic deformation obtained from the rubbing and mechanical action of the rotating tool are used to join metallic materials. FSW provides lot of advantages including fine microstructure, low residual stress and distortion, absence of porosity, cracking and filler

material, easy to automate the process etc. FSW was fruitfully used to weld pure and alloys of aluminum, magnesium and copper [17]. There is a renewed interest in the last decade to apply FSW technology to weld high melting point materials such steels [18], nickel alloys [19] and titanium alloys [20]. The major challenge was imposed on the design of the tool to endure high temperature and wear. Various tool materials including pure tungsten, tungsten alloyed with rhenium, cobalt and lanthanum, tungsten carbide, polycrystalline boron nitrate, silicon nitrate, iridium and molybdenum were used [21,22].

Some research works on FSW of titanium alloy Ti-6Al-4V were documented in literatures recently [23-32]. Buff et al. [23] joined 3 mm thick Ti-6Al-4V sheets using W-Re tool and developed finite element models to predict phase transformations. Wang et al. [24] joined 2.5 mm thick Ti-6Al-4V sheets using W-La₂O₃ and WC-Co tools and measured tool wear. They observed plastic deformation and fracture failure in respectively W-La₂O₃ and WC-Co tools. Wang et al. [25] joined 2.5 mm thick Ti-6Al-4V sheets using W-La₂O₃ tool and investigated the influence of tool pin geometry on tensile deformation of the joints. Zhou et al. [26] joined 2 mm thick Ti-6Al-4V sheets using W-Re tool and analyzed the texture component of the stir zone. Edwards and Ramulu [27] joined 6 mm thick Ti-6Al-4V plates using W-La tool and tracked the material flow using W and Re powder as tracer material. They further applied post weld heat treatment and estimated the fatigue behavior [28]. Yoon et al. [29] joined 2 mm thick Ti-6Al-4V sheets using WC tool and clarified the role of tool rotational speed on the microstructure evolution in the stir zone. Wu et al. [30] joined 2 mm thick Ti-6Al-4V sheets using W-Re tool and demonstrated superior superplasticity of the lamellar microstructure formed in the stir zone. Yoon et al. [31] joined 5 mm thick Ti-6Al-4V plates using Co based alloy tool and studied the microstructural evolution below β transformation temperature. Ji et al. [32] joined 2.5 mm thick Ti-6Al-4V sheets using W-Re tool. They assessed the effect of back heating of the plates during FSW

on microstructure and tensile behavior. Back heating improved tool wear but reduced tensile strength due to higher heat input.

The present work is focused on joining 3 mm thick Ti–6Al–4V sheets using a lanthanated tungsten alloy tool and to characterize the joints using conventional and advanced characterization techniques under various welding conditions. The microstructure evolution is correlated to the tensile deformation behavior.

2. Experimental procedure

3 mm thick mill annealed titanium alloy Ti–6Al–4V sheets were considered for this research work. The dimensions of each plate were 110 mm x 300 mm. The composition is furnished in Table 1. Square butt welding of Ti–6Al–4V sheets was accomplished using an industrial purpose FSW machine (**I-STIR**) as depicted in Fig. 1. All parameters including torque, axial force, and spindle speed can be recorded during welding. The traverse speed was varied from 40 mm/min to 200 mm/min in steps of 80 mm/min. The tool rotational speed (500 rpm) and tilt angle (1.5°) were maintained constant for all joints. A tool made of lanthanated tungsten alloy (W–1%La₂O₃) was used for joining. The tool was designed to have a shoulder diameter of 14 mm and a pin length of 2.9 mm. The pin diameter was tapering from 7 mm at shoulder end to 5 mm at free end. Haynes 230 alloy was used as backing plate. A special shielding arrangement was used to avoid oxidation of the top and bottom surface. Argon was used as shielding gas. The tool head had an internal cooling system. All the joints were made by position control mode. Typical welded plate at a traverse speed of 120 mm/min is shown in Fig. 2.

Specimens were machined perpendicular to the welding direction for metallographic analysis. They were mounted (STRUERS Citopress), polished (STRUERS Labopol) and etched with Kroll's reagent. The etched specimens were observed using an optical microscope (OLYMPUS BX51M). The macrograph was recorded using a stereo microscope

(OLYMPUS SZX16). Electron backscatter diffraction (EBSD) of the weld nugget was carried out in a FEI Quanta FEG SEM equipped with TSL-OIM software. The microhardness was recorded using a microhardness tester (Future Tech FM-700) at 500 g load applied for 15 s across the joint line at the centre of the thickness direction. The tensile specimens were machined according to ASTM: E8M-13a standard having a gauge length of 100 mm, a gauge width of 12.5 mm and a thickness of 3 mm. The ultimate tensile strength (UTS) was computed by means of a computerized universal testing machine (INSTRON 8801). The fracture surfaces were observed using field emission scanning electron microscope (CARL ZEISS-SIGMAHV).

3. Results and discussions

Typical weld seam appearance in Fig. 2 at a traverse speed of 120 mm/min presents a smooth surface appearance without any oxidation. Oxidation used to discolor the weld bead to bluish appearance. This observation suggests that the special shielding arrangement was effective to prevent oxidation. It is well known that titanium and its alloys are so reactive at elevated temperature. Fig. 3a and 3b show the variation of axial force and torque recorded during welding at a traverse speed of 120 mm/min. The plots show that both the axial force and torque rise steadily during ramping period (15 s) and reaches a steady state. The axial force was varying within a range since welding was carried out at position control mode. The variation was consistent throughout the welding indicating stable welding conditions. The average axial force and torque during welding (excluding ramping and tool retraction) were respectively 7.3 kN and 32.3 Nm.

3.1. Macrostructure of welded joints

Fig. 4 reveals the macrographs of friction stir welded Ti-6Al-4V under various traverse speeds. The cross sections show that the joints were formed completely. The welding was successful under the process parameters and the tool design used in this research work.

The thickness of the stir zone was constant and there is no evidence of thinning of sheets. The macrographs further depict that there is no significant volume defects such as tunnels, pin holes, worm holes etc. Those defects appeared in the stir zone of Ti-6Al-4V in some studies [3,27,32]. The formation of such defects was attributed to insufficient heat generation and material flow as well as temperature gradient across the stir zone. Absence of volumetric defects suggests that there was adequate frictional heat available for complete plasticization and material flow for proper consolidation. Nevertheless, the joint at a traverse speed of 200 mm/min exhibits lack of penetration and a worm hole at retreating side. This can be correlated to a reduction in plunge depth and lack of consolidation with increased traverse speed. Overall, the stir zone displays a “basin shape” whose width is reducing from shoulder region to root region. The change in width is due to the net result of material flow created by shoulder and pin region. The available material flow decreases across the thickness which results in a reduction in width of stir zone towards root side. It is noticed in Fig. 4 that the stir zone is completely symmetric with respect to the axis of tool rotation. It is difficult to spot symmetric stir zone in friction stir welded aluminum or magnesium alloy. The flow stress of titanium alloy Ti-6Al-4V is significantly higher which helps to stabilize the material flow around the rotating pin. A symmetric stir zone is often characterized by uniform microstructure. The net area of the stir zone reduces with increased traverse speed due to decrease in the residing time of frictional heat for volumetric heating. The increase in traverse speed leads to a reduction in material flow by shoulder shrinking the stir zone. No onion ring structure was noticed in the stir zone. The absence of onion rings suggests that the material flow caused by tool shoulder is remarkable compared to vertical material flow. The welding window and tool design did not favor the formation of onion rings. There are no dark spots or high color contrast or contaminated regions inside stir zone which could probably indicate the presence of tool wear debris [24,31,33]. This observation indicates that the lanthanated

tungsten alloy tool endured the peak temperature reached and hot deformation conditions without significant wear. The macrographs showed regions of various microstructures namely stir zone (SZ), thermomechanically affected zone (TMAZ), heat affected zone (HAZ) and base metal (BM). The regions across the joint line are subjected to different degree of plastic deformation and frictional heat causing the formation of various zones.

3.2. *Microstructure of welded joints*

The optical and SEM micrographs of the various zones of the joints are shown in Fig. 5 and Fig. 6 respectively. Fig. 5a shows the optical micrograph of as received Ti-6Al-4V. It shows the characteristics of milled and annealed structure. SEM image in Fig. 6a presents a clear view of the microstructure which consists of elongated α in addition to transformed β . The darker phase represents elongated α and the brighter phase corresponds to transformed β . The color contrast is reversed in optical micrographs. β phase is located around the grain boundaries. The elongated α grain is a result of partial recrystallization during mill-annealing process. Following steps were carried out to bring the titanium alloy in mill-annealed condition [34]. Primarily, a homogenization treatment is given to bring the alloy completely into β region. Duration of this treatment determine the effective level of homogenization and the prior grain size of β phase. Subsequently, the alloy is cooled to room temperature and heated again to two phase ($\alpha + \beta$) region. Deformation is exerted on the alloy during this stage. The applied strain is inadequate to complete the recrystallization causing elongated α grains in the base alloy. Fig. 5b records the micrographs of the transition zone showing the microstructure variation from HAZ to SZ. An enlarged view of the HAZ at a traverse speed of 40 mm/min is revealed in Fig. 6b. A comparison between BM (Fig. 6a) and HAZ (Fig. 6b) confirms the growth of β phase after welding. It suggests that the temperature was high enough to induce the growth of β phase. A portion of α phase was transformed into β phase. Small TMAZ was observed in Fig. 5b. Earlier investigators did not report or observe the

formation TMAZ in friction stir welding of titanium alloys [35,36]. FSW induced not only deformation but also phase transformation in titanium alloys. Hence, it was stated that the phase transformation obscured the existence of TMAZ. Nevertheless, Wu et al. [37] observed a clear formation of TMAZ and presented an exclusive investigation on its microstructure. Fig. 6c shows the microstructure of TMAZ of this study which is composed of $\alpha + \beta$ phases. But, the shearing and stretching action of the rotating tool distorted the microstructure. Figs. 5c,d and e show the variation in the microstructure of the stir zone with increased traverse speed. Quantitative analysis of the grain size is discussed later. The magnified view of the stir zone at a traverse speed of 40 mm/min is presented in Fig. 6d. The stir zone is characterized by fully formed lamellar structure. This observation indicates that the peak temperature prevailed in the stir zone during FSW was above the temperature ($\sim 980^{\circ}\text{C}$) required for complete transformation to β phase i.e. β transus temperature [29,30,32]. The lamellar structure is composed of layers of needle shape i.e. acicular α phase and retained β . The transformation of $\alpha + \beta$ structure of BM into lamellar structure in the SZ is as follows. As the tool advances the area ahead of the tool is preheated. The temperature exceeds the β transus temperature during the time the tool reaches the preheated area. All the existing $\alpha + \beta$ phases are transformed to a single β phase. There is no second phase particle in the titanium alloy to restrict or delay the transformation. The size of prior β grains is governed by the temperature and exposure above β transus limit. Both the factors reduce with increased traverse speed and hence a reduction in prior β grains. The cooling rate is relatively high considering the plate thickness of 3 mm. The increased cooling rate enhances the nucleation of α grains but there is insufficient time for the growth of α grains. Therefore, acicular α grains + retained β grains form a lamellar structure in the stir zone. A fully developed lamellar structure is not observed in Fig. 5d and e. This could be possibly due to reduction in peak temperature and dwell time above β transus with increased traverse speed. Fig. 5f shows the details of the worm hole

observed at the retreating side at a traverse speed of 200 mm/min in Fig. 4c. The worm hole may act as a notch and be a failure initiating site during tensile loading.

A montage of TEM micrographs of the SZ at a traverse speed of 40 mm/min is presented in Fig. 7. It confirms the observation of SEM micrographs. Lamellar structure is fully formed across the SZ. Lamellar structure is advantageous to enhance fracture toughness and delay stress corrosion cracking [38]. Parallel arrangement of acicular α grains and β grains are visible. β grains are sandwiched between the sheets of α grains. Ti-6Al-4V not only experiences dynamic recrystallization but also a phase transformation. Faster cooling rate and shorter residing time confine the growth of α grains. Some investigators observed bimodal microstructure comprising of recrystallized α grains and lamellar structure [20,36]. This result suggests that the peak temperature was well above the two phase region and crossed β transus limit. Hence, a lamellar structure is well pronounced at a traverse speed of 40 mm/min. It is also interesting to note the existence of few dislocations in the acicular α grains. Zhou et al. [20,36] captured transparent acicular α grains in the SZ at various processing parameters. They attributed the non existence of dislocations to absence of deformation behind the tool during cooling stage of welding. However, the severe plastic deformation is large enough in this study to produce dislocation and preserved during cooling. The dislocation density is influenced by the process parameters. The process parameters applied in this study favored the formation of dislocations.

EBSD images of the as received Ti-6Al-4V alloy and at various welded conditions are presented in Fig. 8. The elongated grains in Fig. 8a confirm the SEM observation of elongated α phase. The average grain size is approximately 9 μm . Fig. 9 presents an approximate quantitative analysis of SZ at various traverse speeds. The average grain size is 7.6 μm at 40 mm/min and 5.4 μm at 200 mm/min. The average grain size reduced with an increase in traverse speed. The grain size evolution in Ti-6Al-4V during FSW is a complex

phenomenon owing to the associated allotropic phase transformation. The grain boundaries in Fig. 8b are not having smooth contour due to the evolution of lamellar structure as discussed earlier. On the other hand, more equiaxed and fine grains are observed in Fig. 8c and d. This observation suggests that the formation of lamellar structure at traverse speeds 120 mm/min and 200 mm/min was negligible. This could be due to the peak temperature lower than that of β transus limit. The SZ is filled with more recrystallized α grains and retained β grains. The occurrence of fine grains can be ascribed to dynamic recrystallization. However, the mode of dynamic recrystallization whether it takes place in continuous or discontinuous manner remains a topic of debate and deserves a detailed investigation in future. The presence of dislocations in the TEM micrographs (Fig. 7) suggests that the recovery process was partial. The downward trend in Fig. 9 can be elucidated by taking into account phase transformation, deformation and frictional heat generation. The increase in traverse speed lowers the residing time of frictional heat and the degree of plastic deformation. Frictional heat vies to enlarge the grains while deformation attempts to fragment the newly generated grains. The phase transformation may lead to coarsen the grain size depending upon the prior β grain size and the aspect ratio of acicular α grains. The downward trend suggests that the effect of frictional heat prevailed and provided more contribution compared to deformation and phase transformation. Although higher stirring action is available at 40 mm/min, the phase transformation and higher peak temperature increased the grain size.

3.3. Mechanical properties of welded joints

Fig. 10 shows the microhardness variation across the joints at various traverse speeds. The hardness of the SZ is recorded to be higher to that of BM. There is no large variation in hardness across the SZ. There is no significant softening of the HAZ due to increase in β phase. This can be attributed to lower thickness of the HAZ region which was roughly 35 μm . Some investigators reported softening [20,36] while others reported hardening [32,35] of

SZ in friction stir welded Ti–6Al–4V. Hardness change is influenced by the initial material state, process parameters, microstructure evolution, grain size and dislocation density. The generation of fine grain structure in SZ contributes to an increase in hardness according to well known Hall–Petch relationship. The decrease in grain size with increased traverse speed improves the hardness. The presence of dislocations in SZ results in an increase in hardness. The acicular α grains found in the lamellar structure is usually harder. However, Ti–6Al–4V consists of lower amount of β stabilizers [17]. Hence, the acicular α grains are relatively softer compared to that of recrystallized finer α grains. This is the additional cause for lower hardness at a traverse speed of 40 mm/min.

The variation in UTS of the joints at different traverse speeds is graphically presented in Fig. 11. The trend shows that the tensile strength reduced with increased traverse speed. The UTS was measured to be 1040 MPa and 1028 MPa respectively at 40 mm/min and 120 mm/min. Subsequent increase in traverse speed caused a loss of joint strength. The UTS was found to be 716 MPa at 200 mm/min. The variation in joint strength can be correlated to the hardness variation induced by microstructure evolution and microscopic defects. The joints fabricated at 40 mm/min and 120 mm/min failed away from the joint line at BM (Fig. 12). The increase in the hardness of the SZ caused the joint to fail at BM. FSW joints usually exhibit heterogeneous hardness distribution and the joint fails at the point of minimum hardness. The fracture surfaces of those two joints (Fig. 13a and b) are characterized by a network of uniformly dispersed fine dimples. Those are the characteristics of typical ductile failure. The joint at a traverse speed of 200 mm/min failed at the retreating side of the SZ (Fig. 12). The cause of failure can be zeroed down to the worm hole present at the retreating side of the SZ (Fig. 5f). The worm hole reduced the effective area to bear the tensile load and acted as a crack initiating site by invoking notch effect. The fracture surface shows (Fig. 13c) fine size dimples and the possible crack initiation site is marked. Once the crack is initiated, it

proceeds rapidly to complete the tensile failure and reduces the joint strength. The UTS of as received Ti-6Al-4V alloy was tested to be 1045 MPa. Hence, the joint efficiency is 99.5 % at 40 mm/min and 98.4 % at 120 mm/min.

4. Conclusions

3 mm thick titanium alloy Ti-6Al-4V sheets were effectively joined using a lanthanated tungsten alloy tool and the microstructure and mechanical properties were evaluated under various welding conditions. The conclusions of this investigation are presented as follows.

- The area of the stir zone reduced with increased traverse speed due to reduction in residing time of frictional heat for volumetric heating. Lack of penetration and worm hole defects were observed at a traverse speed of 200 mm/min because of reduction in plunge depth and lack of consolidation. The macrographs showed regions of various microstructures namely stir zone (SZ), thermomechanically affected zone (TMAZ), heat affected zone (HAZ) and base metal (BM). There was no debris observed in the macrographs which suggested insignificant tool wear.
- HAZ showed an increase in β phase after welding due to elevated temperature. TMAZ showed a distorted microstructure of $\alpha + \beta$ phases. SZ showed a fully developed lamellar structure of acicular α grains + retained β grains at 40 mm/min. The peak temperature was above β transus temperature at this welding condition. The rest of joints exhibited a recrystallized α grains without significant lamellar structure. Dislocations were observed in the acicular α grains of lamellar structure.
- The average grain size was estimated to be 7.6 μm at 40 mm/min and 5.4 μm at 200 mm/min. The generation of fine grains was related to dynamic recrystallization. The grain size was influenced by phase transformation, deformation and frictional heat. The downward trend indicated that the effect of frictional heat prevailed over other factors.

- SZ exhibited higher hardness under all welding conditions. The improvement in hardness was attributed to fine grain structure and dislocation density.
- The joint strength was 1040 MPa at 40 mm/min and 716 MPa at 200 mm/min. The higher strength was correlated to hardened SZ and the joints failed at BM. The poor joint strength at a traverse speed of 200 mm/min was due to worm hole defect which acted as stress raiser causing the joint to fail at the SZ.

Acknowledgements

The authors acknowledge the National Department of Science and Technology for funding provided via the National Research Foundation (NRF) and the Advance Metals Initiative (AMI) to support this research. The authors are grateful to eNtsa - Innovation through engineering at Nelson Mandela Metropolitan University, Microscopy Lab at University of Johannesburg, OIM and Texture Lab at Indian Institute of Technology Bombay, PSG Institute of Advanced Studies and The South India Textile Research Association (SITRA) for extending the facilities to carry out this investigation.

References

1. D. Banerjee, J.C. Williams, Perspectives on titanium science and technology, *Acta Materialia*, 61 (2013) 844–879.
2. J.L. Buckner, S.W. Stafford, D.M. Cone, Microstructural characterization of Ti-6Al-4V X-links from the Space Shuttle Columbia, *Materials Characterization*, 131 (2017) 261–265.
3. J. Su, J. Wang, R.S. Mishra, R. Xu, J.A. Baumann, Microstructure and mechanical properties of a friction stir processed Ti-6Al-4V alloy, *Materials Science and Engineering A*, 573 (2013) 67–74.

4. G.D. Wen, T.J.Ma, W.Y.Li, J.L.Li, H.Z.Guo, D.L.Chen, Cyclic deformation behavior of linear friction welded Ti6Al4V joints, *Materials Science and Engineering A*, 597 (2014) 408–414.
5. Z. Yang, B. Qi, B. Cong, F. Liu, M. Yang, Microstructure, tensile properties of Ti-6Al-4V by ultra high pulse frequency GTAW with low duty cycle, *Journal of Materials Processing Technology*, 216 (2015) 37–47.
6. C. Jian-chun, P. Chun-xu, Welding of Ti-6Al-4V alloy using dynamically controlled plasma arc welding process, *Transactions of Nonferrous Metal Society of China*, 21 (2011) 1506–1512.
7. C.J. Tsai, L.M. Wang, Improved mechanical properties of Ti-6Al-4V alloy by electron beam welding process plus annealing treatments and its microstructural evolution, *Materials and Design*, 60 (2014) 587–598.
8. P. Xu, L. Li, C. Zhang, Microstructure characterization of laser welded Ti-6Al-4V fusion zones, *Materials Characterization*, 87 (2014) 179 – 185.
9. A. Gursel, Crack risk in Nd: YAG laser welding of Ti-6Al-4V alloy, *Materials Letters*, 197 (2017) 233–235.
10. X.L. Gao, L. Zhang, J. Liu, J. Zhang, Porosity and microstructure in pulsed Nd:YAG laser welded Ti6Al4V sheet, *Journal of Materials Processing Technology*, 214 (2014) 1316–1325.
11. J. Ahn, E. He, L. Chen, R.C. Wimpory, J.P. Dear, C.M. Davies, Prediction and measurement of residual stresses and distortions in fibre laser welded Ti-6Al-4V considering phase transformation, *Materials and Design*, 115 (2017) 441–457.
12. X. Gao, L. Zhang, J. Liu, J. Zhang, A comparative study of pulsed Nd:YAG laser welding and TIG welding of thin Ti6Al4V titanium alloy plate, *Materials Science and Engineering A*, 559 (2013) 14–21.

13. Y. Guo, M.M. Attallah, Y. Chiua, H. Li, S. Bray, P. Bowen, Spatial variation of microtexture in linear friction welded Ti-6Al-4V, *Materials Characterization*, 127 (2017) 342–347.
14. R. Palanivel, I. Dinaharan, R.F. Laubscher, Assessment of microstructure and tensile behavior of continuous drive friction welded titanium tubes, *Materials Science and Engineering A*, 687 (2017) 249–258.
15. R.S. Mishra, Z.Y. Ma, Friction stir welding and processing. *Materials Science and Engineering R*, 50 (2005) 1–78.
16. R. Nandan, T. Debroy, H.K.D.H. Bhadeshia, Recent advances in friction stir welding—process, weldment structure and properties. *Progress in Materials Science*, 53 (2008) 980–1023.
17. G. Cam, Friction stir welded structural materials: beyond Al-alloys, *International Materials Reviews*, 56 (2011) 1–48.
18. S. Sabooni, F. Karimzadeh, M.H. Enayati, A.H.W. Ngan, H. Jabbari, Gas tungsten arc welding and friction stir welding of ultrafine grained AISI 304L stainless steel: Microstructural and mechanical behavior characterization, *Materials Characterization*, 109 (2015) 138–151.
19. K.H. Song, H. Fujii, K. Nakata, Effect of welding speed on microstructural and mechanical properties of friction stir welded Inconel 600, *Materials and Design*, 30 (2009) 3972–3978.
20. L. Zhou, H.J. Liu, Q.W. Liu, Effect of rotation speed on microstructure and mechanical properties of Ti-6Al-4V friction stir welded joints, *Materials and Design*, 31 (2010) 2631–2636.
21. R. Rai, A. De, H.K.D.H. Bhadeshia, T. DebRoy, Review: friction stir welding tools, *Science and Technology of Welding and Joining*, 16 (2011) 325–342.

22. T. Miyazawa, Y. Iwamoto, T. Maruko, H. Fujii, Friction stir welding of 304 stainless steel using Ir based alloy tool, *Science and Technology of Welding and Joining*, 17 (2012) 207–212.
23. G. Buffa, A. Ducato, L. Fratini, FEM based prediction of phase transformations during friction stir welding of Ti6Al4V titanium alloy, *Materials Science and Engineering A*, 581 (2013) 56–65.
24. J. Wang, J. Su, R.S. Mishra, R. Xu, J.A. Baumann, Tool wear mechanisms in friction stir welding of Ti–6Al–4V alloy, *Wear*, 321 (2014) 25–32.
25. J. Wang, J. Su, R.S. Mishra, R. Xu, J.A. Baumann, A preliminary study of deformation behavior of friction stir welded Ti-6Al-4V, *Journal of Materials Engineering and Performance*, 23 (2014) 3027–3033.
26. L. Zhou, H. Liu, L. Wu, Texture of friction stir welded Ti–6Al–4V alloy, *Transactions of Nonferrous Metal Society of China*, 24(2014) 368–372.
27. P.D. Edwards, M. Ramulu, Material flow during friction stir welding of Ti-6Al-4V, *Journal of Materials Processing Technology*, 218 (2015) 107–115.
28. P. Edwards, M. Ramulu, Fatigue performance of friction stir welded Ti–6Al–4V subjected to various post weld heat treatment temperatures, *International Journal of Fatigue*, 75 (2015) 19–27.
29. S. Yoon, R. Ueji, H. Fujii, Effect of rotation rate on microstructure and texture evolution during friction stir welding of Ti–6Al–4V plates, *Materials Characterization*, 106 (2015) 352–358.
30. L.H. Wu, P. Xue, B.L. Xiao, Z.Y. Ma, Achieving superior low-temperature superplasticity for lamellar microstructure in nugget of a friction stir welded Ti-6Al-4V joint, *Scripta Materialia*, 122 (2016) 26–30.

31. S. Yoon, R. Ueji, H. Fujii, Microstructure and texture distribution of Ti–6Al–4V alloy joints friction stir welded below β -transus temperature, *Journal of Materials Processing Technology*, 229 (2016) 390–397.
32. S. Ji, Z. Li, Y. Wang, L. Ma, Joint formation and mechanical properties of back heating assisted friction stir welded Ti–6Al–4V alloy, *Materials and Design*, 113 (2017) 37–46.
33. L.H. Wu, D. Wang, B.L. Xiao, Z.Y. Ma, Tool wear and its effect on microstructure and properties of friction stir processed Ti–6Al–4V, *Materials Chemistry and Physics*, 146 (2014) 512–522.
34. A.L. Pilchak, W. Tang, H. Sahiner, A.P. Reynolds, J.C. Williams, Microstructure evolution during friction stir welding of mill-annealed Ti-6Al-4V, *Metallurgical and Materials Transactions A*, 2011 (42) 745–762.
35. Y. Zhang, Y.S. Sato, H. Kokawa, S.H.C. Park, S. Hirano, Microstructural characteristics and mechanical properties of Ti–6Al–4V friction stir welds, *Materials Science and Engineering A*, 485 (2008) 448–455.
36. L. Zhou, H.J. Liu, Q.W. Liu, Effect of process parameters on stir zone microstructure in Ti–6Al–4V friction stir welds, *Journal of Materials Science*, 45 (2010) 39–45.
37. L.H. Wu, D. Wang, B.L. Xiao, Z.Y. Ma, Microstructural evolution of the thermomechanically affected zone in a Ti–6Al–4V friction stir welded joint, *Scripta Materialia*, 78–79 (2014) 17–20.
38. M. Grujicic, G. Arakere, B. Pandurangan, A. Hariharan, B.A. Cheeseman, C.F. Yen, C. Fountzoulas, Computational analysis and experimental validation of the friction-stir welding behaviour of Ti–6Al–4V, *Proceedings of the Institution of Mechanical Engineers, Part B: Journal of Engineering Manufacture*, 225 (2011) 208–223.

Table 1 Chemical composition of titanium alloy Ti–6Al–4V.

Element	Al	V	Fe	C	N	O	Ti
wt. %	6.25	4.04	0.19	0.018	0.008	0.18	Balance

Figure Captions

Fig. 1. I-STIR friction stir welding machine (Inset shows a photograph of W-1%La₂O₃ tool).

Fig. 2. An example of a friction stir welded Ti-6Al-4V plates at a traverse speed of 120 mm/min.

Fig. 3. Variation of; (a) axial force and (b) torque during welding at a traverse speed of 120 mm/min.

Fig. 4. Optical macrograph of friction stir welded joints at a traverse speed of; (a) 40 mm/min, (b) 120 mm/min and (c) 200 mm/min.

Fig. 5. Optical micrographs of; (a) Ti-6Al-4V and friction stir welded joints at a traverse speed of; (b) 40 mm/min (transition zone), (c) 40 mm/min (SZ), (d) 120 mm/min (SZ), (e) 200 mm/min (SZ) and (f) 200 mm/min (worm hole).

Fig. 6. SEM micrographs of friction stir welded joints at a traverse speed of 40 mm/min showing; (a) base metal, (b) heat affected zone, (c) thermomechanically affected zone and (d) stir zone.

Fig. 7. TEM micrograph of friction stir welded joints at a traverse speed of 40 mm/min showing; (a)–(d) lamellar structure.

Fig. 8. EBSD (IPF + grain boundary) map of; (a) Ti-6Al-4V and friction stir welded joints at a traverse speed of; (b) 40 mm/min, (c) 120 mm/min and (d) 200 mm/min.

Fig. 9. Effect of traverse speed on grain size of friction stir welded Ti-6Al-4V joints.

Fig. 10. Effect of traverse speed on microhardness of friction stir welded Ti-6Al-4V joints.

Fig. 11. Effect of traverse speed on UTS of friction stir welded Ti-6Al-4V joints.

Fig. 12. Photographs of failed tensile specimens. Numbers indicate the value of traverse speed.

Fig. 13. FESEM micrographs of fracture surfaces of friction stir welded Ti-6Al-4V joints at traverse speed of; (a) 40 mm/min, (c) 120 mm/min and (d) 200 mm/min.

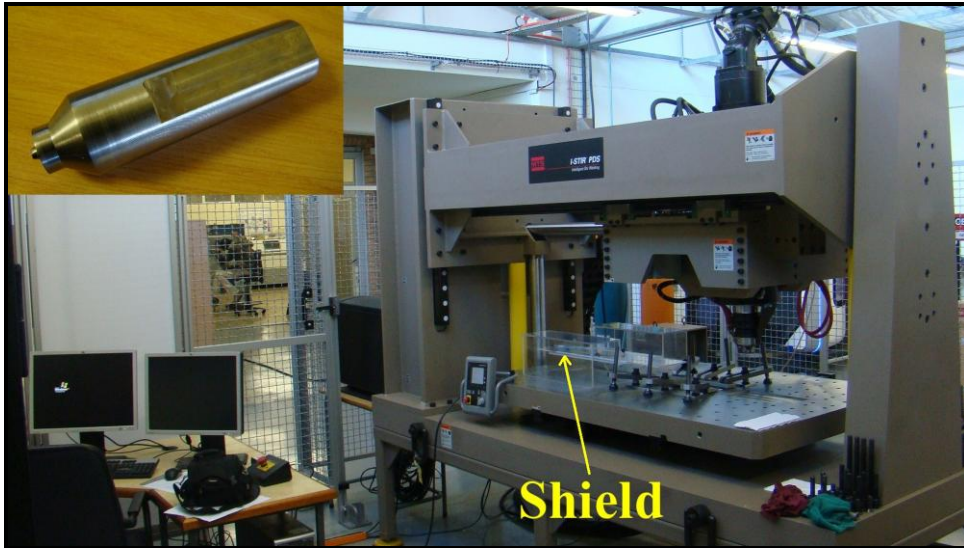


Figure 1



Figure 2

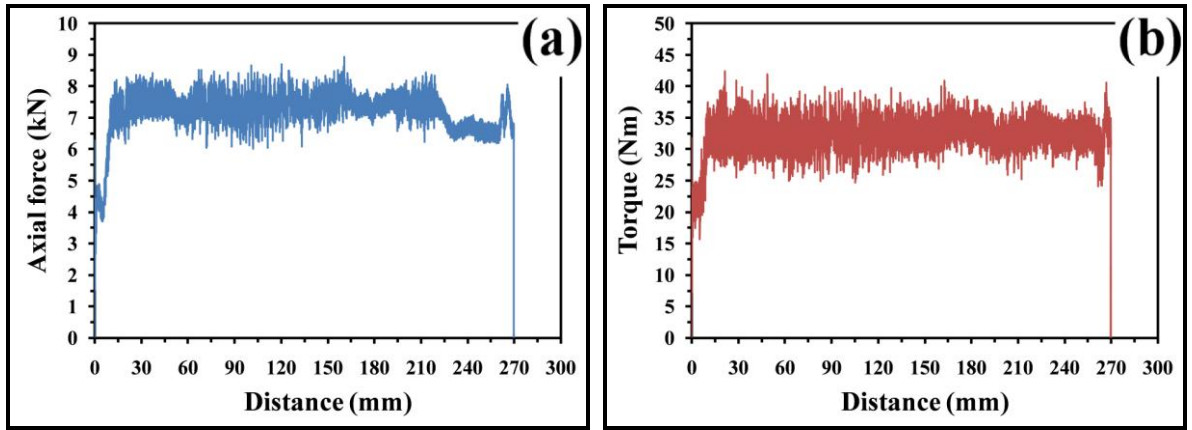


Figure 3

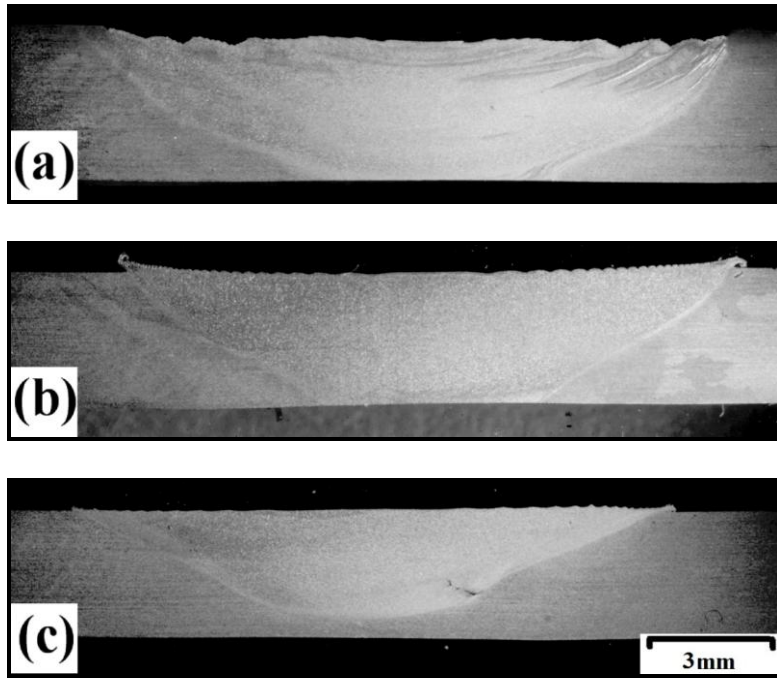


Figure 4

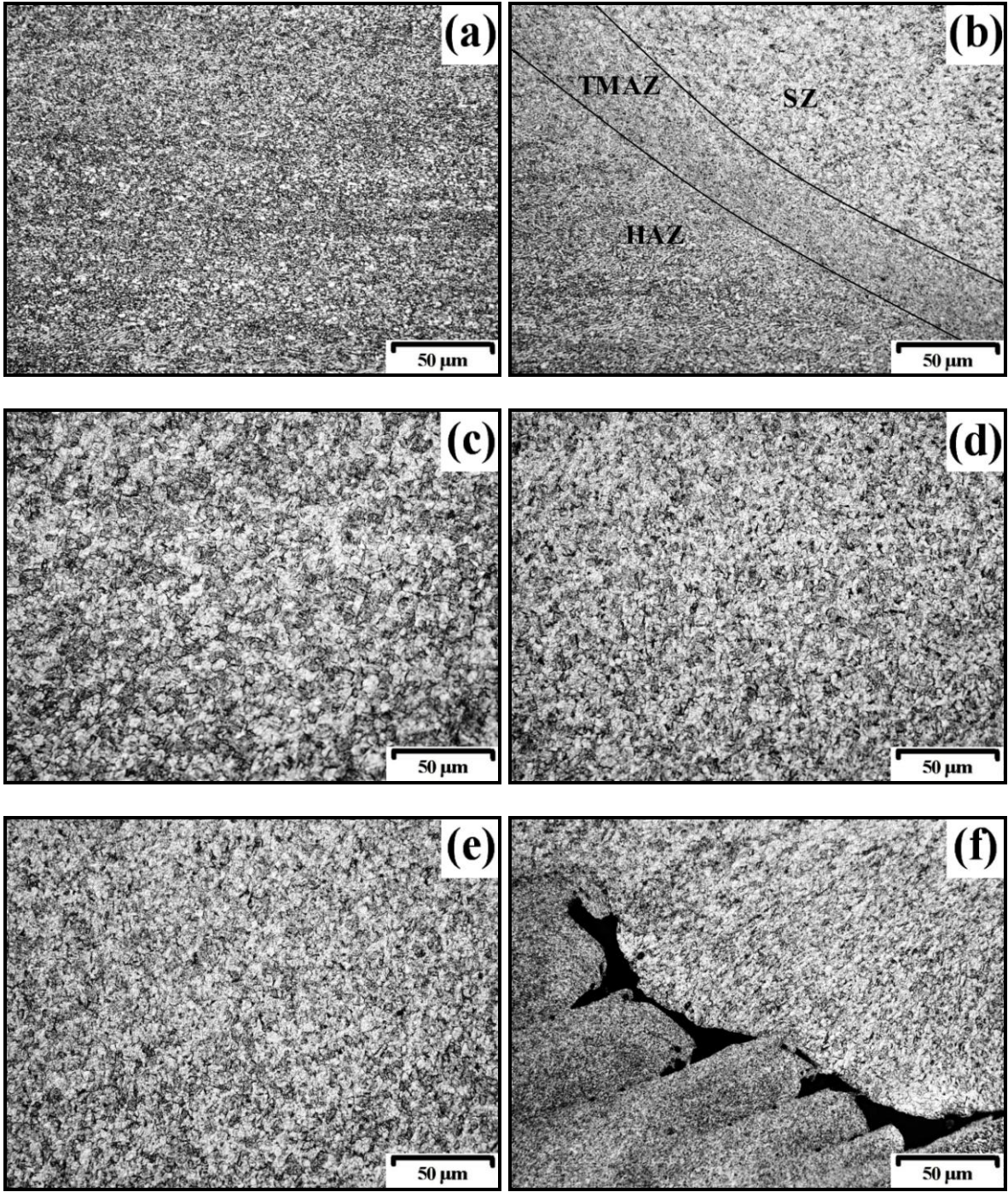


Figure 5

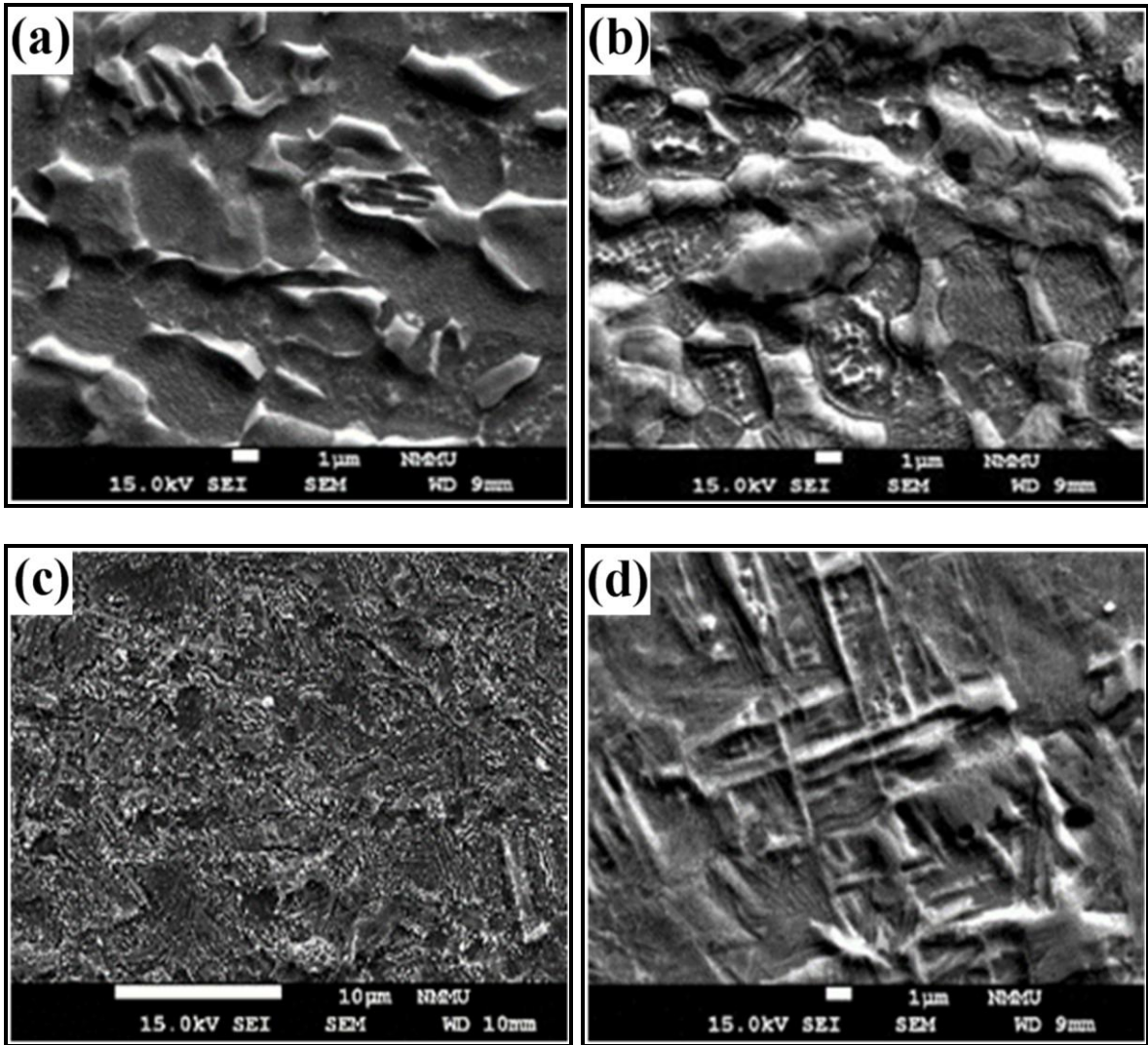


Figure 6

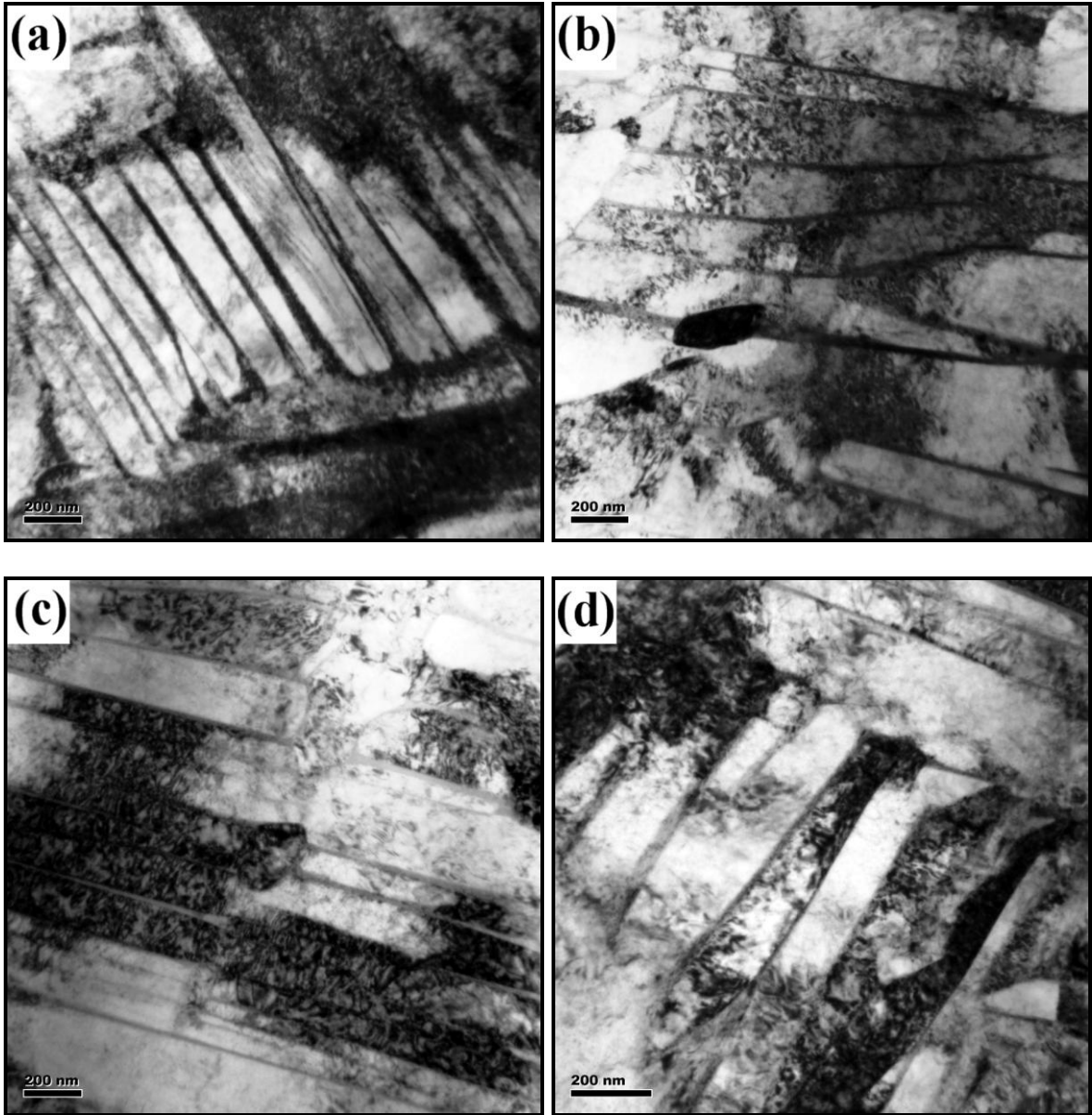


Figure 7

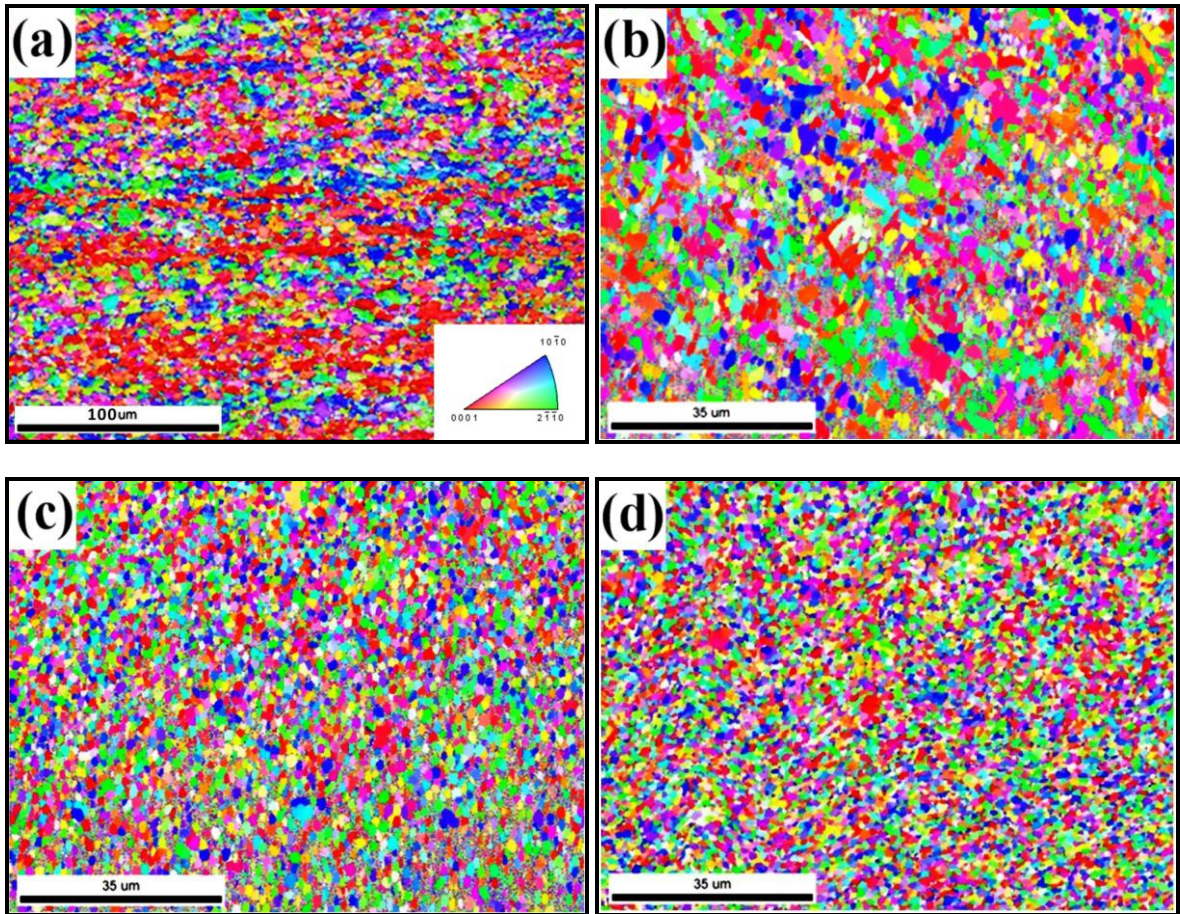


Figure 8

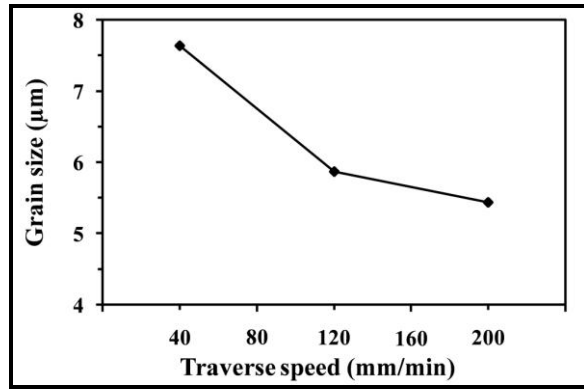


Figure 9

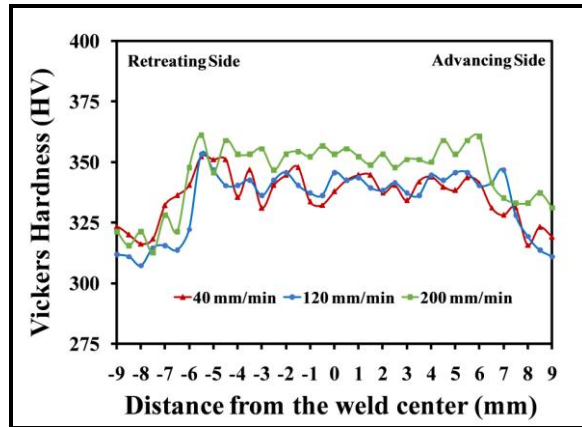


Figure 10

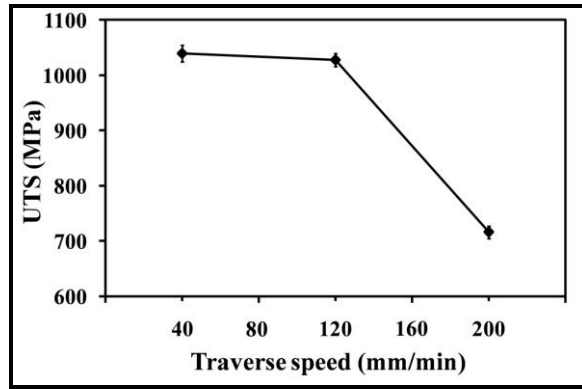


Figure 11

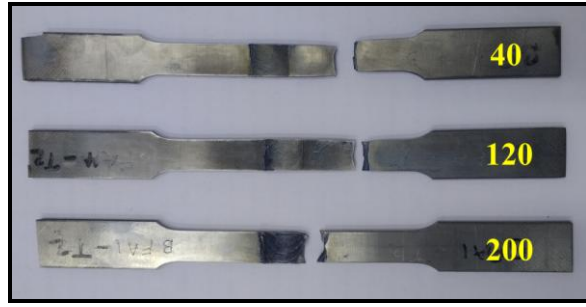


Figure 12

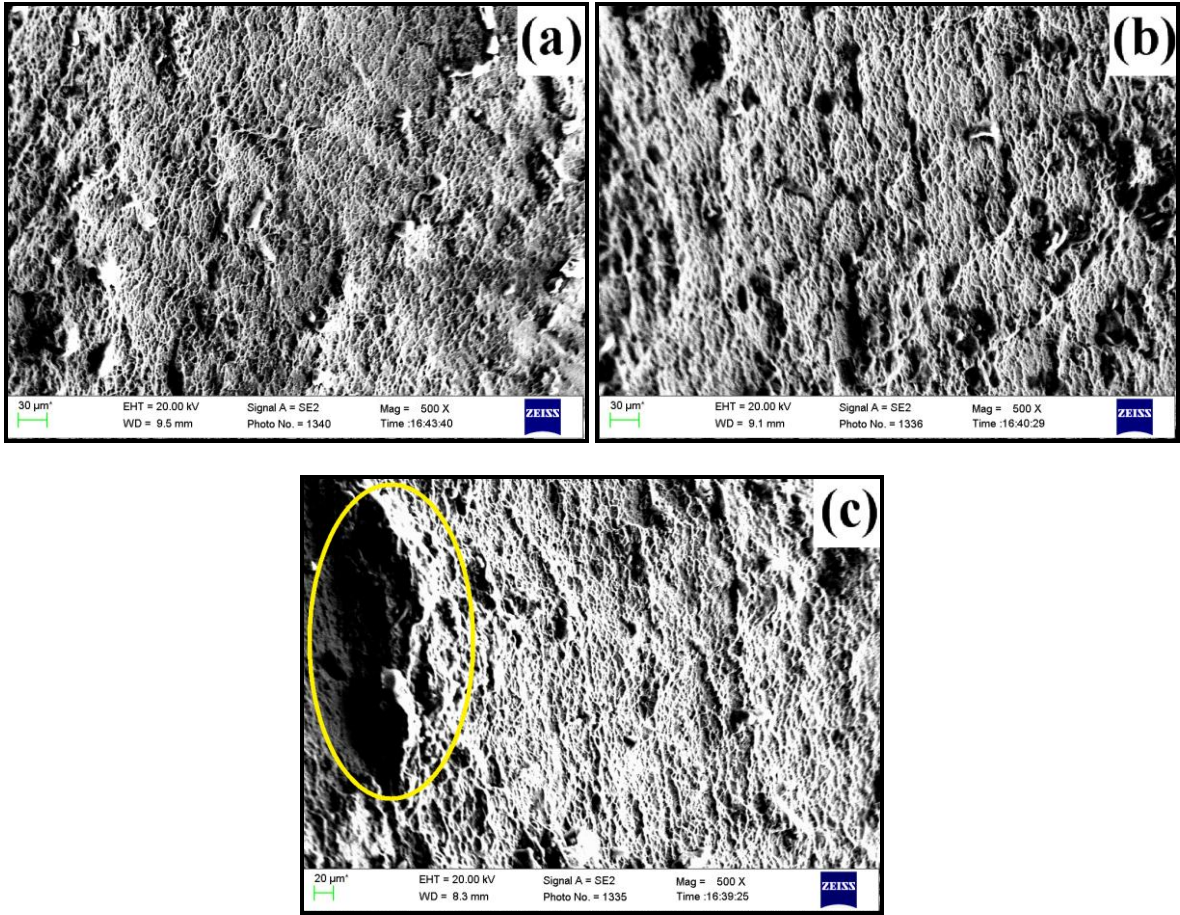


Figure 13